Procedia Manufacturing

Volume 5, 2016, Pages 594–608

44th Proceedings of the North American Manufacturing Research Institution of SME http://www.sme.org/namrc

Femtosecond Laser backside Ablation of Gold Film on Silicon Substrate

Shuting Lei[1*], David Grojo[2], Jianfeng Ma[3], Xiaoming Yu[1], Han Wu[3]

[1]*Kansas State University, Manhattan, KS 66506, USA*
[2]*Aix-Marseille University, CNRS, LP3 UMR 7341, F-13288, Marseille, France*
[3]*Saint Louis University, Saint Louis, MO 63103, USA*
lei@ksu.edu, grojo@lp3.univ-mrs.fr, jma15@slu.edu, philipyu@ksu.edu, hwu12@slu.edu
**contact author: lei@ksu.edu*

Abstract
Femtosecond laser ablation of gold thin film on the front and backside of silicon substrate is investigated, with backside ablation being the focus and front side ablation for comparison. The experiments are performed using 100 fs pulses delivered through an ultrafast laser source combined with an OPA for wavelength conversion at 1300 nm. We create a single shot ablation matrix by varying focus position and pulse energy. The laser beam is characterized using an IR imaging technique at both the front and backside of the substrate. It is found that the pulse profile experiences little distortion after passing though the 1 mm silicon substrate, despite the high pulse energy used. However, a comparison of the front and back ablation site indicates significant attenuation of pulse energy due to nonlinear absorption. Two types of damage happen depending on laser fluence: ablation and burst. Burst damage is confirmed with finite element simulation.

Keywords: Au thin film, silicon substrate, fs laser, laser backside ablation, FEM simulation

1. Introduction

In laser backside ablation, laser pulses propagate through a normally transparent substrate and ablate a thin film material coated on the backside of the substrate. A major application of laser backside ablation is a printing technique referred as laser induced forward transfer (LIFT), as evidenced by the vast amount of work that can be found in the literature. LIFT uses laser pulses to locally transfer a thin film material coated on a transparent support (donor substrate) onto a substrate surface (acceptor substrate). The main purpose is to achieve high quality transferred patterns on the acceptor surface, which is important for applications like printing microelectronics. Another application of laser backside ablation uses laser pulses to selectively remove a thin film material from

 Selection and peer-review under responsibility of the Scientific Programme Committee of NAMRI/SME

doi:10.1016/j.promfg.2016.08.049

the backside of the substrate to generate the desired pattern with high quality. One such example involves backside laser scribing for thin film solar cells, which shows better groove quality compared to front side scribing (Canteli et al., 2013). Despite the different concerns, these two types of backside ablation are governed by similar ablation mechanisms, which depend on material type and operating conditions. Considering the subject matter in this paper, the following discussions focus on laser backside ablation involving metallic materials supported by silicon.

Studies of metallic film transfer (Cu, Ag, Al) using LIFT began almost 30 years ago by Bohandy et al. (1986, 1988) and Schultz and Wagner (1991). They described the whole LIFT process in three stages: material ejection, travel and landing. The dependence of material ejection modes on laser fluence and their influence on the morphology of the deposits on the substrate are main findings in these studies. In recent years, more rigorous numerical analyses (Shugaev and Bulgakova, 2010) and time resolved imaging techniques (Mattle et al., 2012; Pohl et al., 2014; Alloncle et al., 2006) were used to study the ejection dynamics in LIFT. The study by Pohl et al. (2014) for LIFT of 200 nm gold film using picosecond (ps) laser reveals three ejection regimes: droplet ejection at low fluence, jet ejection at medium fluence, and spray ejection at high fluence. Moreover, femtosecond laser seems to have become the main choice of laser source since early 2000s (e.g., Tan et al., 2003), and temporally shaped femtosecond (fs) pulses (double pulses with a time delay) are used in LIFT for Au, Zn and Cr (Klini et al., 2008). It is suggested that the size and morphology may be controlled if the time delay is designed based on the electron-phonon scattering dynamics in these metals.

So far wide band gap dielectric substrates have been used in laser backside ablation because they are transparent to common laser wavelengths. With the development of longer wavelength (>1300 nm) laser radiation sources in recent years, it is natural to ask whether laser backside ablation can be achieved with narrow gap substrates (non-transparent in the visible domain of the spectrum) like silicon. Silicon is a very important material for electronic and photonic devices and it makes no doubt that a demonstration of laser backside ablation through silicon substrate must extend the range of potential applications. Few attempts have been made so far in backside machining of silicon. Using a ns 2 μm fiber laser, Gehlich et al. (2014) demonstrated backside modification of a 500-600 μm thick Si wafer. The modified zone is the result of melting and resolidification. They found a significantly higher damage threshold at the backside compared to the front surface, which is attributed to nonlinear absorption inside silicon. Using a 1552 nm beam, Ito et al. (2014) reported structural modification inside silicon and on the backside of a 320 μm thick silicon wafer. When etched in KOH solution, the modified line on the backside turned into a micrometer deep groove. However, it was not able to machine a groove on the backside directly by laser. In this paper we will concentrate on the ultrafast regime to increase the level of non-linear interaction within the substrate, which may offer a more robust (insensitive to pulse energy fluctuation) and high resolution laser micromachining technique in comparison with machining from the front side, just as that demonstrated in the study by Mercadier et al. (2014) for laser backside ablation through fused silica in a near-filamentary regime.

Accordingly, we present a study of fs laser backside ablation of Au thin film coated on a silicon wafer. We first characterize the beam profile at the back surface after the laser passes through the silicon wafer and compare with that in air. We then conduct backside ablation experiments and compare with results from front side ablation. Finite element method (FEM) is also used to simulate the backside ablation process. Finally, we summarize features of laser backside ablation through silicon in the conclusions.

2. Beam focus characterization in air and through silicon

The beam focus analysis is conducted using the imaging system as shown in Fig. 1. The 1300 nm IR beam coming from the combination of a fs laser (Spectra-Physics, Hurricane) and an OPA (Spectra-Physics 800CF) is focused through a microscope objective with a NA of 0.42. Another

microscope objective with a higher NA of 0.7 (Mitutoyo NIR series) is used to image the focal spot onto an InGaAs camera (Raptor, OWL SWIR 640). The camera directly measures the beam fluence because of its linear response at 1300 nm. The focusing objective is mounted on a motorized stage and indexed at 1 µm between images. The laser repetition rate is 1 kHz and the exposure time is 40 ms for all acquisitions for the IR camera so that each profile relies on an average over 40 laser pulses. Based on calibration procedures (not shown here), we estimate the resolution and dynamic of the measurement are about 1 µm and 19 dB, respectively.

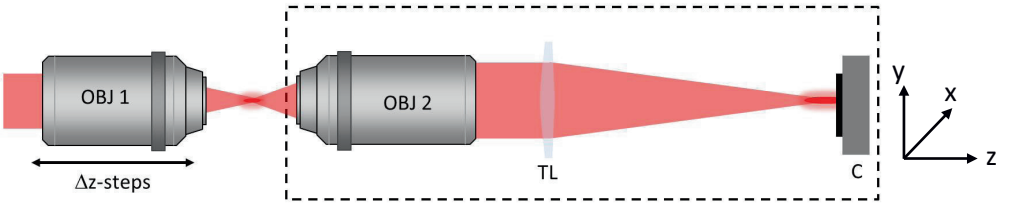

Fig. 1 Experimental setup for beam focus characterization in air. The laser beam is focused with a NA=0.42 microscope objective (OBJ1). A customized microscopy system composed of a microscope objective (OBJ2) and a tube lens (TL) is installed for 100x magnification imaging of the beam profile on an InGaAs camera (C) (Pixel size is 15 µm). By scanning the OBJ1 we can retrieve the 3D fluence distribution in the focal region from the stacked images.

The longitudinal and transverse beam profiles in air are shown in Fig. 2. The pulse energy is about 50 nJ and is below the threshold for air ionization under this focusing condition. With the absence of interaction, the intensity distribution is the exact analog of the measured fluence distribution (no modification of the pulse in the time-domain). The transverse mode of the beam is round with Gaussian-like profile. The measured $1/e^2$ radius is 1.4 µm.

By using the same procedure, we can analyze the beam propagation inside silicon for different incoming pulse energies and then different degrees of nonlinear interaction. The longitudinal profile at the beam focus in air is shown in Fig. 3, together with those inside silicon for various energy levels. The focal volume in air is quite symmetric about the beam waist. When focused inside silicon at low energy, the symmetry tends to breaks down due to spherical aberration. As the pulse energy increases from 10 nJ the distribution becomes severely affected. A contribution to this change is attributed to pre-focal nonlinear absorption as we have measured a threshold for two-photon absorption of ≅ 1 nJ in previous work under similar conditions (Grojo et al., 2013; Leyder et al., 2013). At the pulse energy of 150 nJ used in the backside ablation experiments in this study, the pre-focal absorption is very widespread and takes an elongated shape very similar to the carrot like shape of the damage induced for similar energies inside dielectrics (Grojo et al., 2008), which has inspired high-resolution backside ablation experiments (Mercadier et al., 2014). Here it is important to mention a major difference between dielectrics and semiconductors. In silicon, the critical power for self-focusing is only ≅ 25kW while it is on the order of MW in dielectrics. At energy exceeding 10 nJ we exceed the critical power. Then, despite the strong energy depletion by two-photon absorption that prevents material modification in bulk Si by ultrafast pulses (Mousketaras et al., 2014), self-focusing is likely a contributing factor to the strongly elongated profiles at the highest tested energy (2.3µJ). It should also be noted at this point that we will concentrate on these highly distorted beams when performing backside ablation experiments. We will use the knowledge gained in this section about the focus profile inside silicon in the analysis of the results later in this paper.

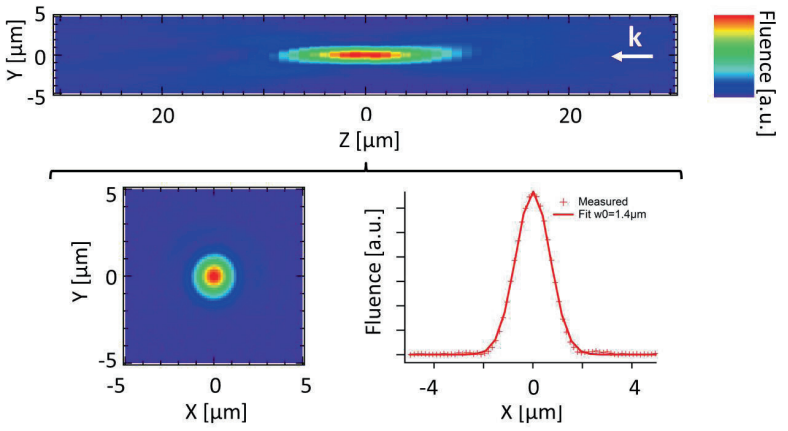

Fig. 2 Beam focus analysis in air revealing a nearly-Gaussian focusing. The top image shows a cross-section of intensity distribution along the optical axis (longitudinal profile). The propagation direction is from right to left. The transverse mode profile is given in the bottom image accompanied with a Gaussian fit from which we extract a beam waist of 1.4 µm.

3. Ablation of gold film on silicon wafer

3.1 Experimental conditions

The experimental setup for laser ablation of gold film is shown in Fig. 4. The output from the 100-fs Ti:Sapphire laser is sent to an OPA to convert the 800 nm beam to 1300 nm (signal). The laser beam is then directed to a dichroic mirror to filter out the idler beam. A half wave plate and polarizer pair is used to adjust beam energy. The beam is cleaned by a high pass filter to stop any residual 800 nm component in the beam before entering the long working distance microscope objective with an NA of 0.42. The objective lens is mounted on a linear translation stage for changing the focal spot position in the propagation direction. The sample is mounted on a XYZ translation stage and moves in the transverse directions. All the stage movements are synchronized with the shutter control, which is triggered by laser pulses at 100 Hz repetition rate to allow single shot illumination of the sample surface in the experiments. The sample is 20 nm thick gold film, deposited on a 1 mm thick silicon substrate using high temperature vacuum evaporation method.

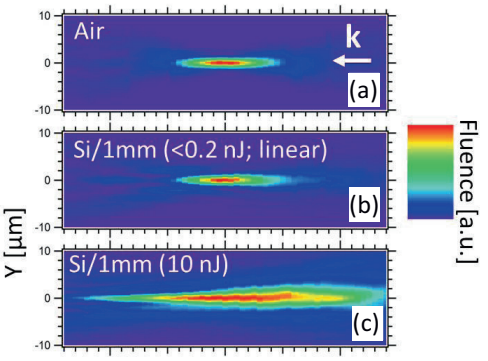

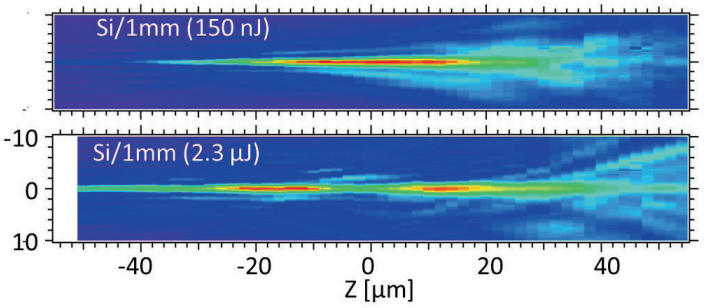

Fig. 3 Beam focus longitudinal profile in air (a) and inside silicon (b-e) for increasing p(d)e energy up to 2.3 µJ. We note a breaking of the symmetric nearly Gaussian focusing at energies exceeding few nano joules.

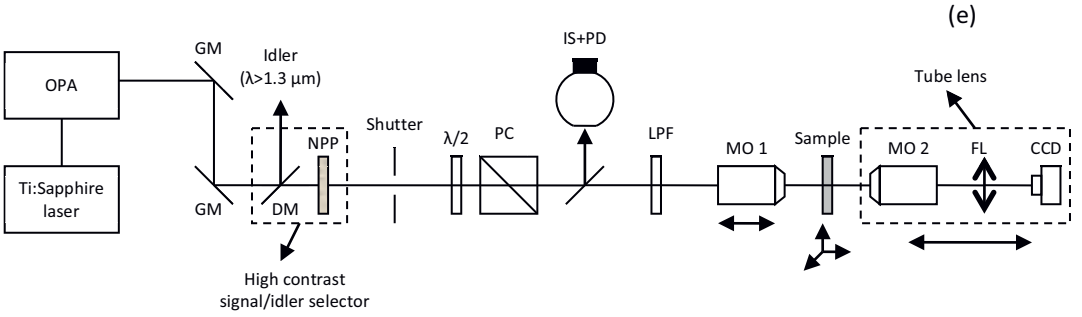

Fig. 4 Experimental setup for laser ablation of gold film. OPA is an optical parametric amplifier, GM gold mirrors, DM a dichroic filter, NPP a nanoparticle polarizer, λ/2 a half-wave plate, PC a polarizing cube, LPF a long pass filter and MO microscope objective. The combination MO2, tube lens (FL) and the camera correspond to the system for focus analysis.

Single shot ablation is conducted from both the front and backside of the silicon substrate. The test pattern shown in Fig. 5 is designed to study the effect of pulse energy and beam diameter on Au film ablation. From the leftmost column moving to the right, each subsequent column sees a decrease in pulse energy by 10% of its maximum value compared to the one immediately to the left. Therefore a 10-column design leads to a pulse energy range of 0.1 to 1.0 E_{max}. From the center row where the beam is focused on the sample surface, moving upwards results in post-focal defocusing and moving downwards results in pre-focal defocusing, because each step corresponds to an increment of 5 µm of the focusing objective in the beam propagation direction. Hence, the beam spot size increases in both ways (in air), and the amount of change in spot size between two adjacent rows can be determined by the movement of the focusing objective. The maximum pulse energy after the microscope objective is 147 and 157 nJ for the front side and backside ablation, respectively.

3.2 Results and discussion

The damage patterns for the gold film are shown in Fig. 6. For the front side ablation (Fig. 6a), a nearly symmetric pattern is observed about the center row where the beam is focused. Moving from

the leftmost column to the right, pulse energy decreases gradually and so is the damage size. Damage to the substrate occurs at some high energy sites as shown, for example, in the inset of Fig. 6a. Moving up or down from the center row, beam size increases gradually. The damage size follows the same trend first until the beam size becomes too large and thus the fluence falls below the damage threshold. The size symmetry about the center row is the result of the symmetry of the beam profile about the beam waist in air (see Fig. 3a).

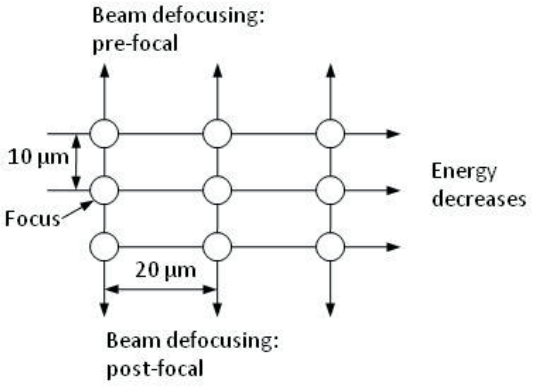

Fig. 5 Single shot laser ablation test pattern. To study the influence of the irradiation parameters, we use an automated procedure creating a matrix of patterns where each line corresponds to a different focusing position (depth) and each row a different energy.

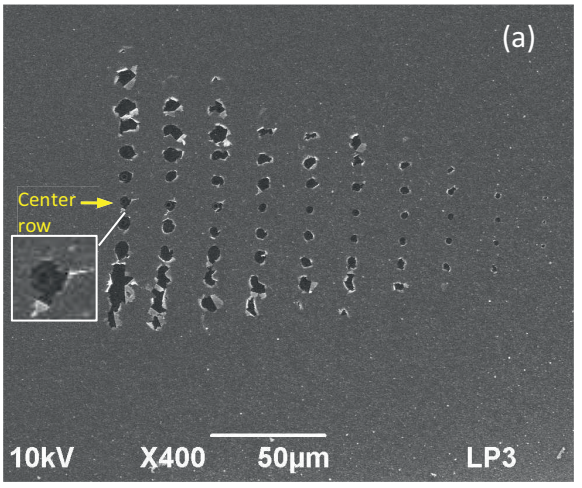

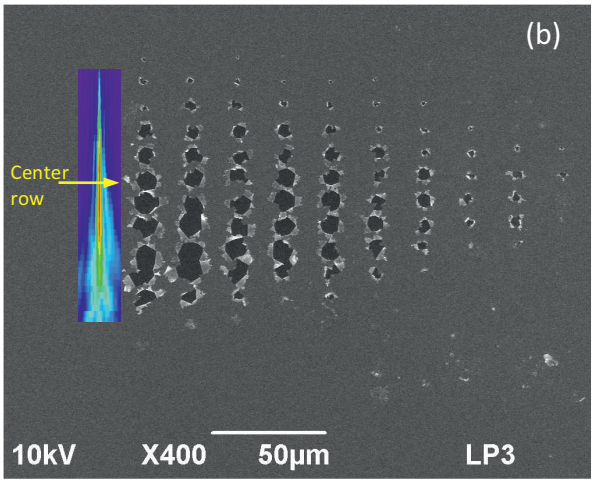

Fig. 6 SEM images showing ablation of Au thin film on silicon wafer from (a) the front side and (b) the backside with pulse energy varying from ≅150 nJ to ≅15 nJ (from left to right).

In contrast, the damage pattern does not exhibit the same degree of symmetry about the center row in the backside ablation as shown in Fig. 6b. Damage size decreases from left to right as expected because of the decrease in pulse energy. The variations of damage size within a column can be explained by the beam propagation profile when focused inside silicon, as shown in Fig. 3d. As a viewing guide, the same beam profile is placed to the left of the first damage column in Fig. 6b. Each damage spot corresponds to a laser intensity and beam diameter on the image at the same vertical location. Therefore, the damage size changes with the beam intensity profile. The fact that damage size decreases towards the beam tip indicates that only the tapering central spot induces damage, and the outside ringsare too weak to cause any damage.

Further, there appear to be two damage modes in the interaction between the laser and the gold film: ablation and burst. Ablation happens when laser fluence is high and above the damage threshold over the laser spot area, and thus the film is removed from the substrate in an explosive manner. This mode of damage normally leaves behind a damage spot with clean boundaries. The three central rows in the front side ablation fall into this category. In this study the ablation threshold is estimated using the following relationship between the square of the damage spot size approximated with a circular diameter (D) and the logarithm of the laser pulse energy (Liu, 1982), where E_{th} = ablation threshold and $2w_o$ = laser spot size.

$$D^2 = 2w_0^{\,2} \ln\left(\frac{E_0}{E_{th}}\right) \qquad (1)$$

A plot of the square of damage diameter, D^2, against the logarithm of energy is made to obtain both the spot size (slope of line) and ablation threshold (the extrapolation of D^2 to zero) (Fig. 7). The damage threshold is found to be 0.11 J/cm^2. Burst is the other damage mode that happens when laser fluence is not high enough to explosively remove the material but the pressure generated at the interface is large enough to break open the film through either initial damage at the center where peak intensity occurs or defects within the thin film. Figure 8 shows an instance where the film is just beginning to break open from the substrate along the grain boundaries. This mode of damage usually creates a large spot with small flakes folding back from the edge like flower petals. Some of the

damage at the front side is the result of burst while almost all of them at the backside take this form of damage.

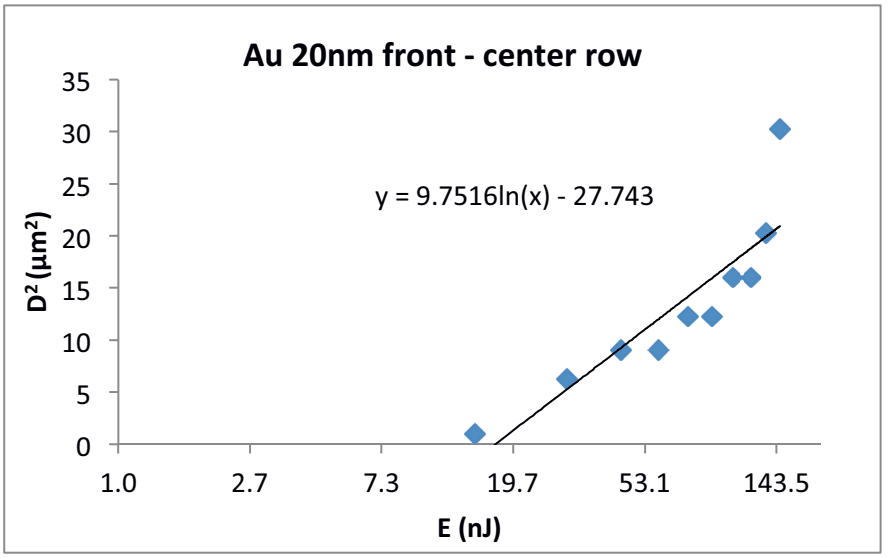

Fig. 7 D-square of the damage spot versus pulse energy in front side ablation.

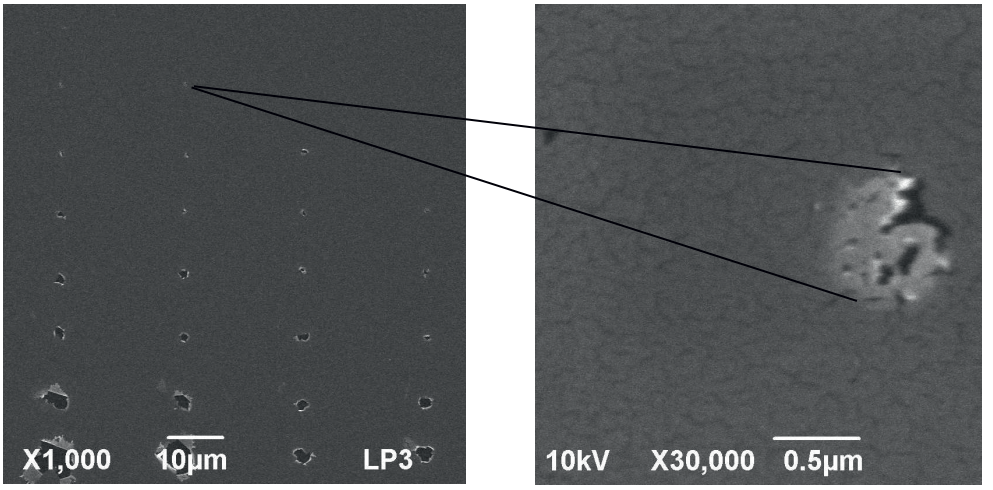

Fig. 8 Illustration of material damage by bursting assisted by defects. The right image is a magnified SEM image of the backside irradiated film at low fluence (modest energy and defocused beam).

4. Finite element simulation of film burst under laser induced pressure

While material damage threshold obtained from laser ablation experiments can be used to predict damage size based on ablation mechanism, it should not be used for the same purpose when damage occurs through burst like in our backside ablation experiments. Therefore, in this study, we attempt to use finite element method (FEM) to simulation the film burst process, which, once verified, can be used to guide the selection of laser parameters for the backside ablation process.

4.1 FEM model

In this research, the commercial FEM software Abaqus is used to model film delamination using the traction separation mechanism at the interface between a 20 nm gold film and an 833 nm silicon substrate, which is implemented using cohesive elements in the simulation. The thickness of the cohesive elements layer is 5 nm. Figure 9 below illustrates of silicon side laser ablation model for gold film.

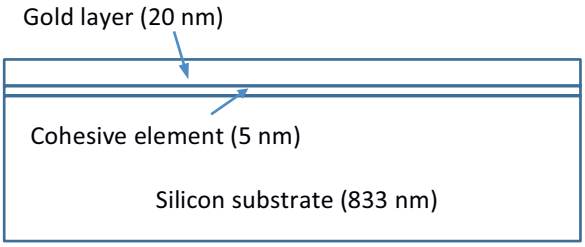

Fig. 9 Femtosecond laser back side ablation model.

The Young's moduli of elasticity and Poisson's ratios for gold film and silicon substrate are given in Table 1 (CES EduPack, 2011). The plastic properties of the gold film and material properties of ductile damage model for gold film are shown in Table 2 (Timpano K., 2005) and Table 3, respectively. The damage evolution law for the gold film can be specified in terms of equivalent plastic displacement, which is 0.2 nm in this research.

Table 1 Material property for gold film and silicon substrate

Properties	Value
Young's modulus of gold	75 GPa
Poisson's ratio of gold	0.42
Mass density of gold	19.3 g/cm^3
Young's modulus of silicon substrate	72 GPa
Poisson's ratio of silicon substrate	0.22
Mass density of silicon	2.3 g/cm^3

Table 2 Plastic property of gold film

Yield stress (MPa)	Plastic strain
200	0
240	0.7
275	1
275	1.1
270	1.2

Table 3 Material property for ductile damage model for gold film

Fracture strain	Stress Triaxiality	Strain rate
0.123	1.424	0.001
0.154	1.463	0.001
0.189	1.501	0.001

Because laser induced plasma expansion at the gold film/silicon interface can delaminate the gold film from the substrate, traction separation behaviors at the interface are modeled using cohesive elements. The elastic moduli in the normal direction and the first and second shear directions are 28000, 14000, and 14000 kPa, respectively. Maximum nominal stress criterion is used to describe damage initiation of the cohesive elements, which means that Damage is assumed to initiate when the maximum nominal stress ratio ($\max\left\{\frac{\langle t_n \rangle}{t_n^0}, \frac{t_s}{t_s^0}, \frac{t_t}{t_t^0}\right\} = 1$) reaches a value of one. The t_n^0, t_s^0, and t_t^0 represent the peak values of the nominal stress when the deformation is either purely normal to the interface or purely in the first or the second shear direction, respectively. The value $\langle t_n \rangle$ is 0 if $t_n < 0$ and t_n if $t_n > 0$ because a pure compressive deformation or stress state does not initiate damage. The peak values of the nominal stress t_n^0, t_s^0, and t_t^0 are 0.1MPa, 0.1MPa, 0.1MPa, respectively. The damage evolution law for the cohesive elements can be specified in terms of equivalent displacement, which is 1 nm in this research.

4.2 Laser induced pressure at the gold-silicon interface

Because the pulse duration is so short, the absorbed laser energy is confined in the focal volume and heat diffusion to the surrounding area is negligible. It is assumed that the deposited energy is converted into vapor pressure at the gold-silicon interface. The distributed pressure induced by the laser over the irradiated area is estimated based on the following equation, adapted from Eq. (6.59) in Gamaly (2011),

$$P(r) = \frac{AF(r)}{t} \times \left(1 - \exp\left(-\frac{2t}{\delta}\right)\right) \quad (2)$$

where A is absorption coefficient, t is film thickness, δ is optical penetration depth, and F(r) is distributed laser fluence. For a Gaussian beam, the distributed fluence over a laser spot area is given by

$$F(r) = 2F_a \exp\left(-\frac{2r^2}{r_0^2}\right) \quad (3)$$

where r_0 is beam radius and F_a is average laser fluence. The known parameter values are listed in Table 4. A and δ are determined based on data from the Refractive Index Database (Polyanskiy, 2015). To obtain the beam radius r_0, the transverse intensity distribution is approximated with a Gaussian profile, and the radius at which the intensity drops to 60% of its peak value is used to specify the beam size in this study. Because of the difficulty in determining the energy loss in the silicon substrate, the average laser fluence incident on the gold film after passing through the silicon wafer is measured using our imaging setup and a calibration of the pixel response in air. For the pulse energy of 157 nJ incident on the front surface we found that the laser fluence yielded at the backside is only 0.035 J/cm^2, which is assumed to be absorbed by the gold film.

Table 4 Parameters for estimating laser induced pressure

t (nm)	A	δ (nm)	r_0 (μm)	F_a (J/cm^2)
20	4%	25	1.5	0.035

In Fig. 10 below (same image as in Fig. 6b), the 6th hole from the top of the first column is used to validate the numerical model by comparing the experimental diameter and numerical diameter of the hole. Then the diameters of the 5th and 7th hole are predicted using the validated model and the numerical results are compared with the measured values from the image.

It should be noted that for the 6th hole, $P(r) = 28\times e^{-0.9\times r^2}$ and the beam radius is $r_0 = 1.5\ \mu m$. For the 5th hole, $P(r) = 21\times e^{-1.65\times r^2}$, and the beam radius is $r_0 = 1.1\ \mu m$. For the 7th hole, $P(r) = 20\times e^{-0.32\times r^2}$, and the beam radius is $r_0 = 2.5\ \mu m$. For all these equations for P(r), r is in μm and P(r) is in GPa.

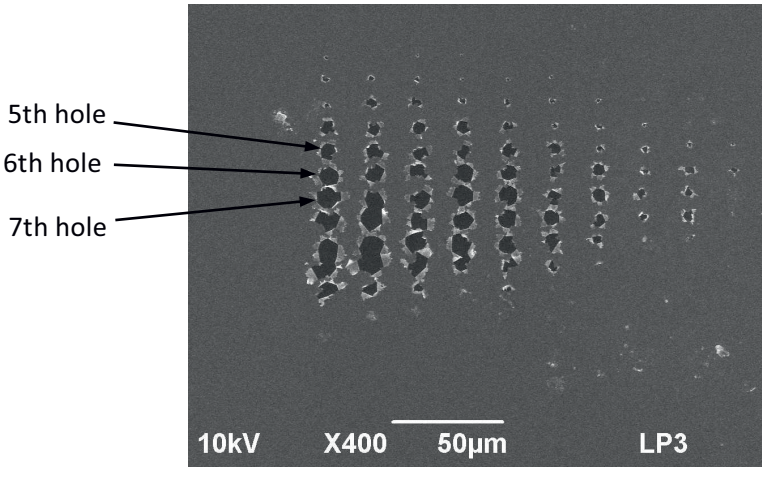

Fig. 10 The illustration of the three holes that are modeled and simulated using FEM.

4.3 Simulation results and discussion

In the FEM modeling, Gaussian-distributed pressure is applied at the interface between the cohesive layer and gold film. It should be noted that only half of the gold film and substrate is modeled because of the symmetry. This means that the left vertical edge of the FEM model is the center line of the laser beam. Explicit time-stepping scheme is used for modeling this laser-induced highly dynamic process. In experiments, the pulse duration is 100 fs. In simulation, the laser-induced pressure will maintain its distribution and magnitude for a longer time period until the gold film fractures. In this research, different durations of laser-induced pressure have been investigated and we found that 300 fs can ensure the fracture of the gold film. Hence, throughout this research, 300 fs is selected as the duration of laser-induced pressure. It should also be mentioned that because 300 fs is a very short time as opposed to the time for gold film to come to a complete state of fracturing and deformation, 1 ns is used for the total time period of simulation.

Fig. 11 shows the film bursting process in response to laser induced stress at the interface through simulation. The simulation begins with the gold film firmly bonded to the silicon substrate by a thin layer of cohesive elements (Fig. 11a). Fig. 11b depicts an instance in the middle of the simulation where film delamination occurs and fracture starts to develop within the gold film. At the end of the simulation as shown in Fig. 11c, the film bursts and the pressure is released. The film debris resulting from the rupture can be seen clearly. In addition, delamination of the gold film from the substrate is also very obvious. Because laser induced pressure at the film-substrate interface peaks at the center of the laser spot, the von Mises value is the highest close to the center of the laser beam, which is about 210 GPa. The predicted diameter of the 6th hole in Fig. 10 is 3.68 um × 2 =7.36 um.

The measured diameter for the 6th hole is 7.81um. The error between the experimental diameter and the numerical one is 5.76%. This means that the numerical model is accurate and may be used to predict the diameters under other ablation conditions. As a demonstration, the numerical model is used for predicting the diameters for the 5th and 7th hole in Fig. 10, and the simulation diameters are found to be 5.86 and 8.21 um, respectively. The experimental diameters for these two holes are 6.25 and 8.59 um, respectively. A comparison between the predicted and experimental values is shown in Fig. 12. The model seems to underestimate the damage size in all three cases, but the errors are all within 7%.

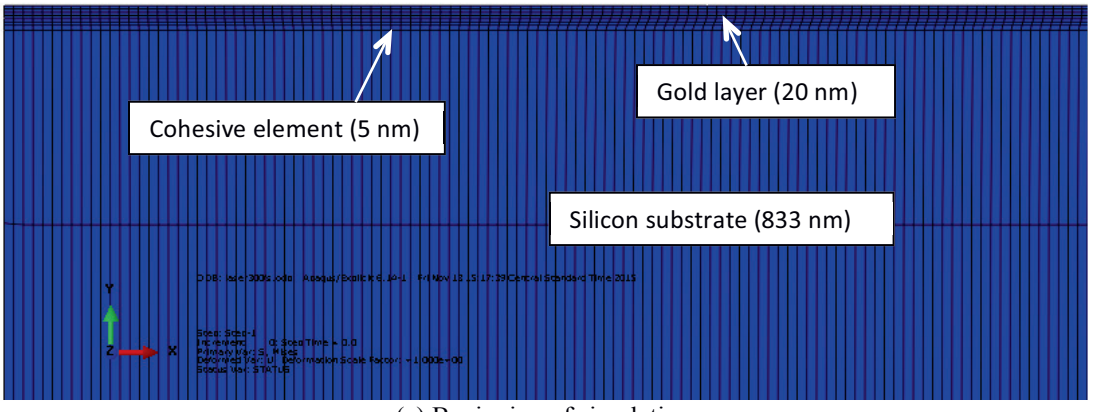

(a) Beginning of simulation

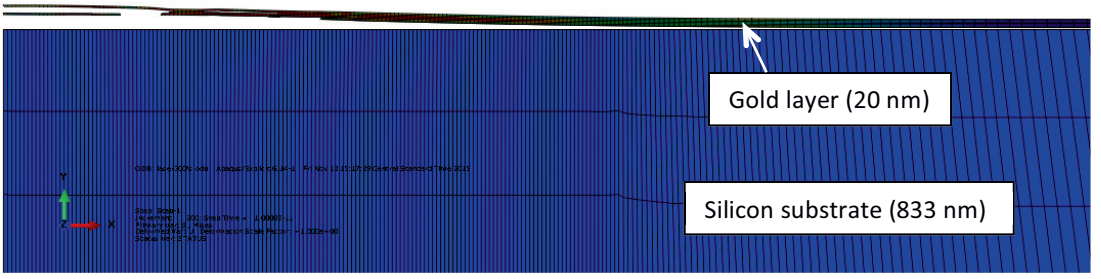

(b) Middle of simulation

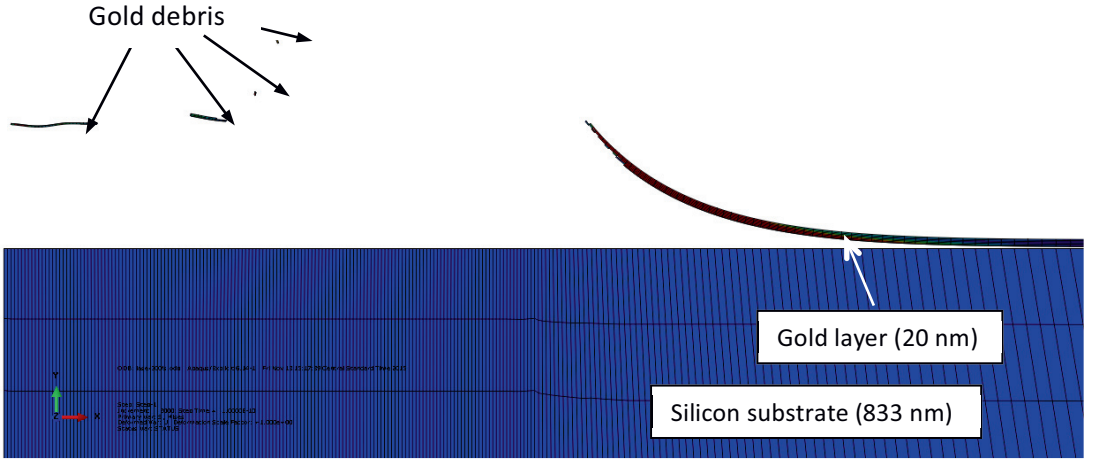

(c) End of simulation

Fig. 11 Progression of film bursting process under fs laser induced pressure (6th hole in Fig. 10).

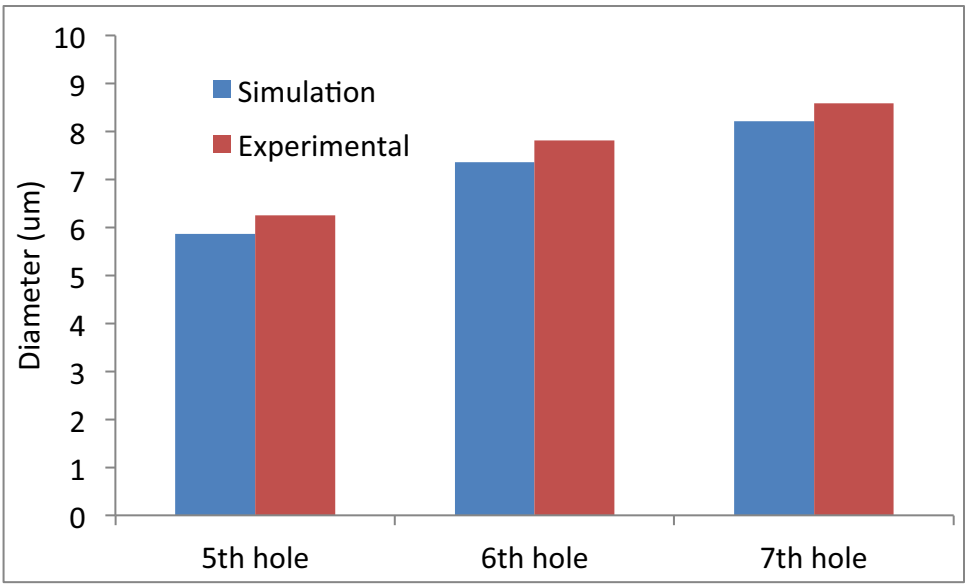

Fig. 12 Comparison of experimental and simulation results for three holes indicated in Fig. 10.

5. Conclusions

Femtosecond laser ablation of gold film on silicon substrate is conducted and the findings from this study are summarized below.

- Laser beam maintains its transverse mode well even after passing through a 1 mm thick silicon wafer. The longitudinal profile becomes needle-like as the beam propagates through the material, which is caused by nonlinear absorption in the pre-focal region and potentially self-focusing and laser-induced microplasma interaction. Significant loss in transmitted energy is measured because of the nonlinear absorption.
- Ablation damage occurs when laser intensity is high enough and is observed in the front side ablation of the 20 nm thick gold film. Burst damage occurs almost exclusively in the backside ablation due to low laser intensity. The threshold for burst damage depends on the strength and defects of the deposited film. Grain boundary seems to serve as crack initiation point for film burst under laser irradiation.
- FEM simulation is able to verify the burst mode of damage from the experiments. It shows that the formation of burst damage is caused by film rupture at the central portion of the laser spot and delamination toward the edge. FEM can be used to predict the damage size caused by film burst.

6. References

Alloncle AP, Bouffaron R, Hermann J and Sentis M. Experimental study of front and back ablation of metal thin film using ultrashort laser pulses. In: *Proceedings of SPIE,* 2006, 6261: 626127 (7).

Bohandy J, Kim BF and Adrian FJ.Metal deposition from a supported metal film using an excimer laser. Journal of Applied Physics, 1986, 60(4): 1538-1539.

Bohandy J, Kim BF, Adrian FJ and Jette AN. Metal deposition at 532 nm using a laser transfer technique. Journal of Applied Physics, 1988, 63(4): 1158-1162.

Canteli D, Torres I, García-Ballesteros JJ, Cárabe J, Molpeceres C and Gandía JJ. Characterization of direct- and back-scribing laser patterning of SnO_2:F for a-Si:H PV module fabrication. Applied Surface Science, 2013, 271: 223-227.

CES EduPack, version 7.0, 2011.

Gamaly EG.The physics of ultrashort laser interaction with solids at non-relativistic intensities. Physics Reports, 2011, 508: 91-243.

Gehlich N, Bonhoff T, Sisken L, Ramme M, Gaida C, Gebhardt M, Mingareev I, Shah L and Richardson C. Utilizing the transparency of semiconductors via "backside" machining with a nanosecond 2 μm Tm: fiber laser. In: *Proceedings of SPIE,* 2014, 8968: 89680W (7).

Grojo D, Leyder S, Delaporte P, Marine W, Sentis M and Utéza O. Long-wavelength multiphoton ionization inside band-gap materials. Physical Review B, 2013, 88: 195135(5)

Grojo D, Gertsvolf M, Jean-Ruel H, Lei S, Ramunno L, Rayner DM and Corkum PB. Self-controlled formation of microlenses by optical breakdown inside wide-band-gap materials. Applied Physics Letters, 2008, 93: 243118 (3).

Ito Y, Sakashita H, Suzuki R, Uewada M, Luong KP and Tanabe R. Modification and machining on back surface of a silicon substrate by femtosecond laser pulses at 1552 nm. Journal of Laser Micro/Nanoengineering, 2014, 9(2): 98-102.

Klini A, Loukakos PA, Gray D, Manousaki A and Fotakis C. Laser induced forward transfer of metals by temporally shaped femtosecond laser pulses. Optics Express, 2008, 16(15): 11300-11309.

Leyder S, Grojo D, Delaporte P, Marine W, Sentis M and Utéza O. Non-linear absorption of focused femtosecond laser pulses at 1.3 μm inside silicon: independence on doping concentration. Applied Surface Science, 2013, 273: 13-18.

Liu JM. Simple technique for measurements of pulsed Gaussian-beam spot sizes. Optics Letters, 1982, 7(5): 196-198.

Mattle T, Shaw-Stewart J, Schneider CW, Lippert T and Wokaun A. Laser induced forward transfer aluminum layers: Process investigation by time resolved imaging. Applied Surface Science, 2012, 258: 9352-9354.

Mercadier L, Rayner DM and Corkum PB. Control of femtosecond laser ablation of thin films from a dielectric surface by nonlinear interaction with the substrate. Physical Review Applied, 2014, 2: 034001(6).

Mouskeftaras A, Rode AV, Clady R, Sentis M, Utéza O and Grojo D. Self-limited underdense microplasmas in bulk silicon induced by ultrashort laser pulses. Applied Physics Letters, 2014, 105: 191103 (4).

Pohl R, Visser CW, Römer GRBE, Sun C, Huisin't Veld AJ and Lohse D. High-resolution imaging of ejection dynamics in laser-induced forward transfer. In: *Proceedings of SPIE,* 2014, 8967: 89670X (7).

PolyanskiyMN. Refractive index database. Available at http://refractiveindex.info (accessed August 2015).

Shugaev MV and Bulgakova NM.Thermodynamic and stress analysis of laser-induced forward transfer of metals. Applied Physics A, 2010, 101: 103-109.

Schultze V and Wagner M. Laser-induced forward transfer of aluminum. Applied Surface Science, 1991, 52: 303-309.

Tan B, Venkatakrishnan K and Tok KG. Selective surface texturing using femtosecond pulsed laser induced forward transfer. Applied Surface Science, 2003, 207: 365-371.

Timpano K. Mechanical characterization of gold thin films for RF-MEMS. In: *Proceedings of Virginia Space Grant Consortium Student Research Conference,* 2005.